



HAL
open science

Experimental mesoscopic investigation of the local cyclic plasticity of a non-oriented electrical steel

Jeremie Bouquerel, C. Schayes, Jean-Bernard Vogt

► To cite this version:

Jeremie Bouquerel, C. Schayes, Jean-Bernard Vogt. Experimental mesoscopic investigation of the local cyclic plasticity of a non-oriented electrical steel. *Materials Science and Engineering: A*, 2021, *Materials Science and Engineering: A*, 820, pp.141454. 10.1016/j.msea.2021.141454 . hal-03259323

HAL Id: hal-03259323

<https://hal.univ-lille.fr/hal-03259323v1>

Submitted on 13 Jun 2023

HAL is a multi-disciplinary open access archive for the deposit and dissemination of scientific research documents, whether they are published or not. The documents may come from teaching and research institutions in France or abroad, or from public or private research centers.

L'archive ouverte pluridisciplinaire **HAL**, est destinée au dépôt et à la diffusion de documents scientifiques de niveau recherche, publiés ou non, émanant des établissements d'enseignement et de recherche français ou étrangers, des laboratoires publics ou privés.



Distributed under a Creative Commons Attribution - NonCommercial 4.0 International License

1 **Experimental mesoscopic investigation of the local cyclic plasticity** 2 **of a non-oriented electrical steel**

3 **J. Bouquerel*, C. Schayes, J.B. Vogt**

4 Univ. Lille, CNRS, INRAE, Centrale Lille, UMR 8207 -
5 UMET - Unité Matériaux et Transformations, F-59000 Lille, France

6 *Corresponding author : jeremie.bouquerel@centralelille.fr

7 **Abstract**

8 Complementary mesoscopic investigations have been carried out on a notched specimen, made
9 of Fe-3%Si steel and submitted to fatigue loading. Load control fatigue testing was conducted to
10 ensure localised cyclic deformation and the resulting displacement fields were measured by means of
11 Digital Image Correlation (DIC). Electron Channelling Contrast Imaging (ECCI) and Electron Back-
12 Scatter Diffraction (EBSD) complete the DIC data by giving a different view of the local plasticity, as
13 they image the dislocation structure and map their related characteristics, such as misorientation.

14 Hence, two misorientation based criteria, namely Grain Reference Orientation Deviation (GROD)
15 and Grain Orientation Spread (GOS) were considered for EBSD analysis. Based on a previous study, a
16 $\langle \text{GOS} \rangle - \Delta \varepsilon_t$ abacus has been coupled with a $\langle \text{GOS} \rangle$ - DIC abacus in order to evaluate locally the
17 encountered strain field and link this latter to an equivalent total strain variation. The obtained
18 results have been discussed from the evolution of the dislocations structures, as observed by ECCI.

19 This combination of mesoscopic techniques clearly emphasizes the local deformation by means of
20 both qualitative and quantitative measurements. On one hand, DIC and EBSD measurements indicate
21 the presence of strain localisation which can be correlated to a certain level of cyclic strain
22 amplitude. On the other hand, the variation of the strain levels and its distribution when moving
23 away from the notch are confirmed by the dislocation structures evolution seen by ECCI. Such

24 structures vary from cells, vein and channels and entangled dislocations regions as the analysed
25 areas go away from the notch.
26 At a local scale, the DIC measurements behave as numerous virtual extensometers while its
27 combination with EBSD and ECCI data confirms the correlation with the accumulated cyclic strain.

28 **1. Introduction**

29 Nowadays, the knowledge and the understanding of the plasticity phenomena remain fantastic
30 challenges for both engineers and researchers. On one hand, it allows the design of materials and/or
31 components that exhibit superior mechanical properties by optimising their microstructure and by
32 improving thermomechanical treatments to which those latter are submitted. On the other hand, it
33 allows a lifetime optimisation as materials may undergo various types of constraints when in
34 operating conditions.

35 One of the constraints which has a high occurrence concerns the fatigue loading, which can be
36 related to expected or unexpected in-service conditions. Indeed, fatigue corresponds to the
37 progressive and structural damage that occurs when a material is subjected to cyclic loading. It is a
38 major cause of component failure in many industrial domains such as construction [1,2], energy [3–5]
39 and transportation [6–10].

40 The Fe-3%Si steel (M330-35A) is of prime interest in regards with the industrial sectors mentioned
41 above. As it belongs to the non-oriented electrical steels, it is frequently used for its electrotechnical
42 properties obtained by a well-controlled combination of chemical composition, grain-based features
43 (morphologic and crystallographic texture) and sheet thickness (350 μm). It is then particularly
44 adapted to rotating machines such as alternators.

45 This steel and more generally the iron-silicon electrical steels have been specifically optimised for
46 their electrical properties and more precisely for the prediction of core losses to improve electrical
47 machine design [11–14], but less their mechanical properties. Nevertheless, the rotor design

48 improvement requires now to clearly know their mechanical properties and more precisely their
49 fatigue properties.

50 Within the last decades, metallurgists and mechanical engineers have developed robust
51 characterisation tools to characterise the plastic deformation that occurs during fatigue. Although
52 the synergies and tools were initially different, the frontier between their approaches become more
53 and more narrow. Indeed, metallurgists pay more attention to microstructural developments ranging
54 from more or less complex dislocation interactions to more mesoscopic misorientation build-up. To
55 their side, the mechanical community evaluated deformation in terms of stresses and strains and
56 part of them are focusing on microstructural impact through micromechanics.

57 Several interesting tools may then be considered for investigations at the mesoscopic and
58 macroscopic scales. Electron Back-Scatter Diffraction (EBSD) and Electron Contrast Channelling
59 Imaging (ECCI) bring valuable information regarding deformation as it can be viewed from
60 microstructural evolution. Digital Image Correlation (DIC) gives quantitative data regarding the strain
61 and stress field at various scales. Finally, simulation based on Finite Element Modelling (FEM), arises
62 to predict or validate materials and component behaviours.

63 All those techniques take benefits from a constant development brought from their respective
64 community, which give a more precise ability for the plastic deformation analysis [15–24]. When
65 regarding their applications to fatigue behaviour, those approaches are often used separately [25–
66 27], although few recent works tried to perform some correlation [24,28–31]. However, only a
67 fragmentary view of the material characteristics is treated in order to describe mechanisms related
68 to crack initiation or first steps of crack propagation by focusing on.

69 The purpose of the present work is somehow different. Two previous studies performed on the
70 fatigue behaviour of the M330-35A steel point out the ability of EBSD and ECCI to give mesoscopic
71 details allowing the explanation of the stress response of the material to strain cycling [32,33]. It was
72 also shown that, depending on the applied strain, this steel exhibits behaviours corresponding to low

73 temperature and high temperature regimes. Moreover, EBSD based criteria pointed out the
74 associated strain localisation that leads to crack initiation. In the present study, those results are
75 used as a kind of abacus in order to estimate the fatigue strain encountered during the cyclic loading
76 of a notched sample. The comparison between the SEM based analysis and the DIC measurements
77 validates the previous approach on a sample with a more complex shape, for which both stress and
78 strain distribution is heterogeneous. Mesoscopic DIC measurements gives a large amount of local
79 virtual extensometers for the different areas of the sample, while EBSD/ECCI confirm the
80 encountered strain levels assess the presence of dislocations cells.

81 **2. Material and experimental procedure**

82 **2.1. Material**

83 The material considered in this study is the M330-35A of the EN10106 classification (or graded as
84 36F185 according to ASTM A677). This corresponds to a non-oriented silicon steel with the chemical
85 composition given in Table 1.

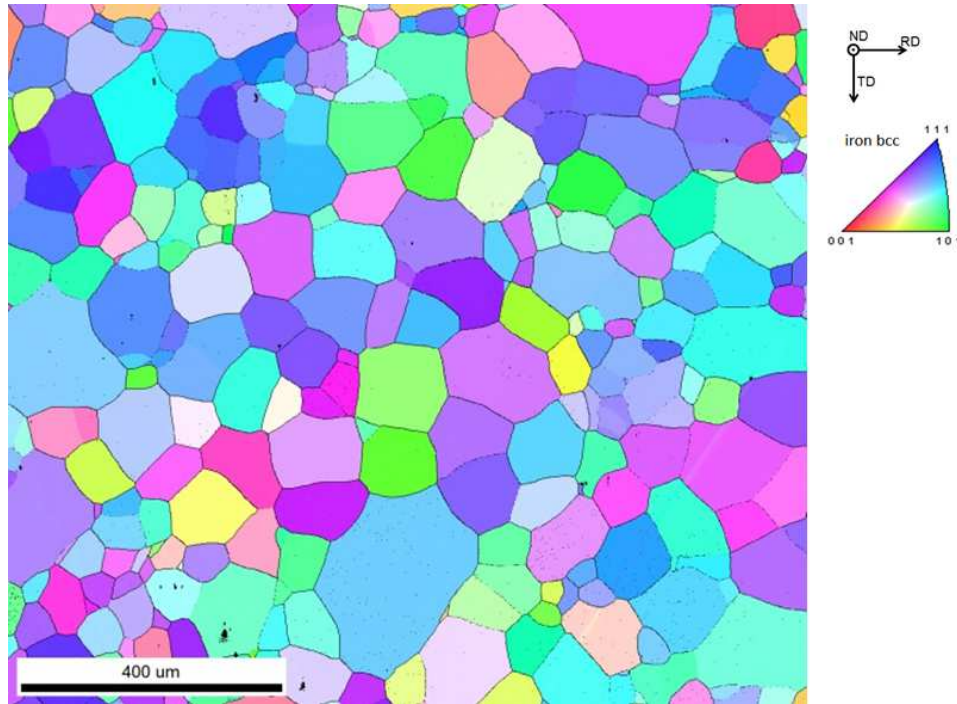
86 **Table 1: Chemical composition of the M330-35A steel (wt%)**

Elements	C	Mn	P	Si	S	Al	Fe
wt%	0.003	0.109	0.011	2.884	0.004	0.448	Bal.

87
88 The material has been provided in thin sheet, 350 μm in thickness, but no details regarding the
89 rolling conditions have been given by the supplier. It exhibits a ferritic structure (Figure 1) with a
90 wide grain size distribution [32–34]. The average grain size determined by the intercept method is 75
91 μm . The sheet thickness corresponds therefore to a thickness of 4 to 5 grains. The grains are not
92 randomly oriented but are assumed to show a $[1\ 1\ 1] // \text{ND}$ fibres, resulting from recrystallization as
93 suggests the literature on iron silicon steels [35,36]. The ideal texture for non-oriented silicon steel is
94 $(001) [uv0]$ where each grain has two $\langle 1\ 0\ 0 \rangle$ directions in the sheet plane, and the properties are
95 nearly isotropic but no industrial process has been developed to obtain this ideal structure yet [37].

96 M330-35A is a soft and ductile material with a Young modulus $E=186$ GPa and an elongation to
97 fracture $A=28\%$.

98



99

100 **Figure 1: Microstructure of the M330-35A steel**

101

102 **2.2. Fatigue tests**

103 In the previous studies, the main idea was to perform conventional Low Cycle Fatigue (LCF) tests on
104 smooth specimen to understand the behaviour of the M330-35A steel. In the present case, the
105 purpose is double. By making a notch in a flat sample, this reproduces a shape feature of a real
106 component and ensure stress concentrators which may modify the local strain levels.

107 The LCF tests were carried out on a MTS servo-hydraulic machine on the same shape used in the
108 previous investigations unlike the introduction of a rounded notch at the mid place of an edge of the
109 gage length. With this specimen shape (cf. figure 2.a), it is not relevant to perform strain controlled
110 LCF tests. Hence, a load control ranging from 0 to 700 N in a push-pull mode and with a triangular
111 wave form was used instead.

112 **2.3. Digital Image Correlation (DIC)**

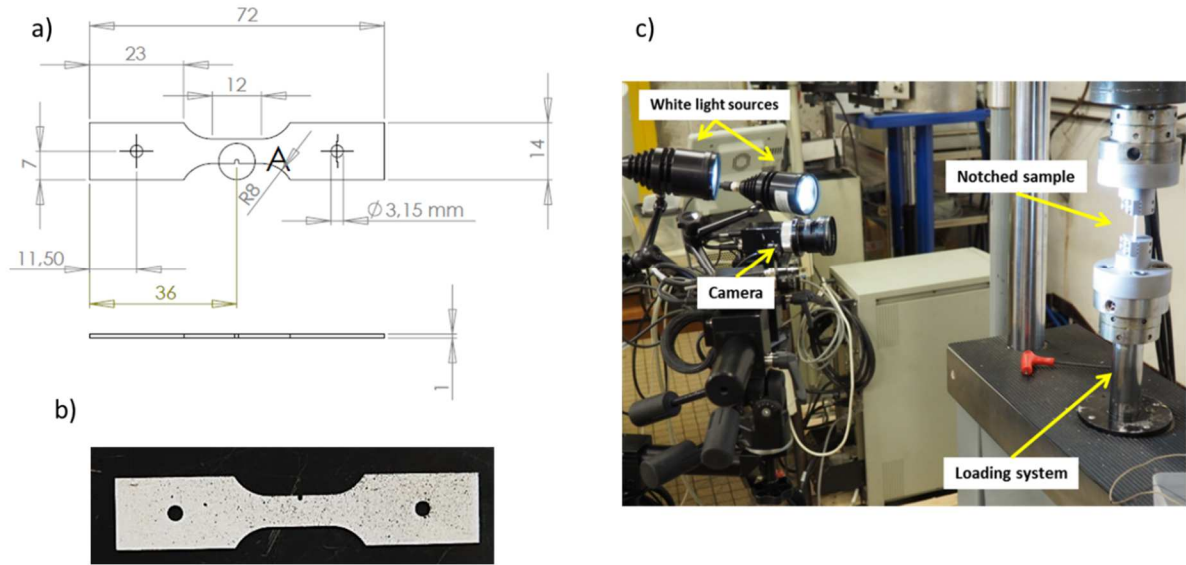
113 The DIC analysis, which consists in an advanced non-contact optical technique for displacement
114 measurement, has been performed on a 2D system from GOM system (Gesellschaft für Optische
115 Messtechnik). The considered system is constituted of a CCD camera, fitted with a 100mm lens, has a
116 resolution of 2448*2050 pixels and a maximum frame rate of 15Hz. The post-processing of the data
117 was performed with ARAMIS® v6.3.0. software (GOM mbH, Braunschweig, Germany).

118 To conduct the DIC analyses, the notched specimen was first mechanically polished up to 3µm. Then,
119 to obtain a speckle surface, a white antireflection paint was applied uniformly on the surface. Once it
120 was dry, a graphite-based spray is applied in order to obtain correct grey distribution from the
121 random repartition of black dots on the surface (Figure 2b). This preparation is crucial in order to
122 have enough contrast and pattern features that allows to perform comparative analysis. [38,39]

123 The sample was then put into the fatigue testing machine and the camera was placed in front of the
124 specimen at 90° to its surface (Figure 2c).

125 Image acquisition was performed before the fatigue test and during the cycle number N=1, 10, 11,
126 50, 100, 500, 1000 and 2000. The framerate acquisition, coupled with a strobe effect, allows to
127 acquire around 30 snapshots per cycle.

128 Thanks to those patterns acquisition, the residual strain field in the unloading state has been
129 evaluated by comparing the DIC data taken at the minimum stress at each fatigue cycles in
130 comparison to the reference image taken before the fatigue test.



131

132 **Figure 2: (a) Dimensions of the notched sample, (b) Speckle surface of a notched sample and (c) experimental set-up**

133 **2.4. Electron Back Scatter Diffraction**

134 EBSD analysis have been carried out on a FEI Quanta 400 scanning electron microscope fitted with an
 135 Oxford Instruments EDS/EBSD system. The purpose was to obtain EBSD pattern which processing
 136 provides localisation of the strain at a mesoscopic scale.

137 A Nordlys CCD camera was used for pattern acquisition. Data were recorded at $1 \mu\text{m}$ step size using
 138 Oxford Instruments Aztec software. The analyses were carried out using both Oxford Instruments
 139 Channel 5 and TSL OIM 7 commercial software. By choosing the highest possible image resolution for
 140 pattern processing and by optimising the Hough transform parameters, an angular resolution of
 141 about 0.3° has been measured. As the grain size of the studied steel is relatively large, the considered
 142 step size for acquisition ($1 \mu\text{m}$), has been chosen according to the Chen *et al.* optimization method
 143 [40]. The observations were made on zones of $800 \mu\text{m} \times 450 \mu\text{m}$ in the centre of the useful area of
 144 the fatigue samples.

145 The local strain levels of the Fe-3Si steel were considered through the Image Quality (IQ) of the
 146 pattern and the study of local misorientation. As kernel and grain based approaches have been fully
 147 investigated in a previous work [32], two criteria are considered here, respectively GROD and GOS as

148 they provide more evidences of the local strain. Those criteria, which belong to the grain-based
149 approach, are detailed hereafter.

150 Grain Reference Orientation Deviation (GROD) is based on the misorientation between a reference
151 point of that grain and the other points. The reference point can be the mean misorientation of the
152 grain or the point of the grain where the KAM is the lowest. Note that the KAM value is defined as
153 the mean value of misorientation a pixel and its neighbours providing that misorientation does not
154 exceed 5°, which should correspond to a Low Angle Grain Boundary (LAGB). It is defined by equation
155 (1-2).

$$GROD_i = \omega_{ik} \quad (1)$$

156 With ω_{ik} the deviation angle between orientation of pixel I and reference orientation of grain k.
157 This GROD criterion is sensitive to the orientation heterogeneities that evolve during deformation.

158 Grain Orientation Spread (GOS) is based on the misorientation averaged on the whole grain and is
159 defined by equation (5-4). In this mode each point in the grain is shaded with the same colour in the
160 maps.

$$GOS_k = \frac{1}{M} \sum_{i=1}^M GROD_i \quad (2)$$

161 With M the numbers of pixel within the grain k.

162 Here, the GOS criterion indicates the grains, as defined by orientation parameters, for which the
163 orientation heterogeneities are the most important.

164 **3. Results and discussion**

165 **3.1. DIC displacement field measurements**

166 As mention previously, the residual displacement field in the deformed image was estimated with
167 the Aramis software by comparison with the initial image of the non-deformed state. From this first
168 set of data, the strain along the Y axis (i.e. loading axis), ε_Y , and shear strain, ε_{XY} were then calculated

169 at each stage. The strain distributions at F_{\max} are shown in Figure 3 as a function of the number of
170 cycles. Strain was measured with an error of 0.1%.

171 These results highlight the longitudinal strain localisation at the notch root and the shear bands and
172 the shear strain in the shear bands. Due to the subset size (9 pixels), which corresponds to a DIC
173 spatial resolution of 210 μm , the strain distribution in the exact vicinity of the notch cannot be
174 precisely evaluated.

175 The evolution of the longitudinal strain ε_y at the point where the strain is the maximum at the notch
176 root was also evaluated and reported in Figure 4a and 4b.

177 Figure 4a shows that the cyclic evolution of the longitudinal strain is in agreement with the cyclic
178 load, the strain increases when the force increases. Moreover, the maximum strain increases with
179 the number of cycles up to $N=500$ cycles. From this number of cycles, the strain evolution is in a
180 stabilised regime where no more plastic straining occurs as shown in the hysteresis curves (figure
181 4b).

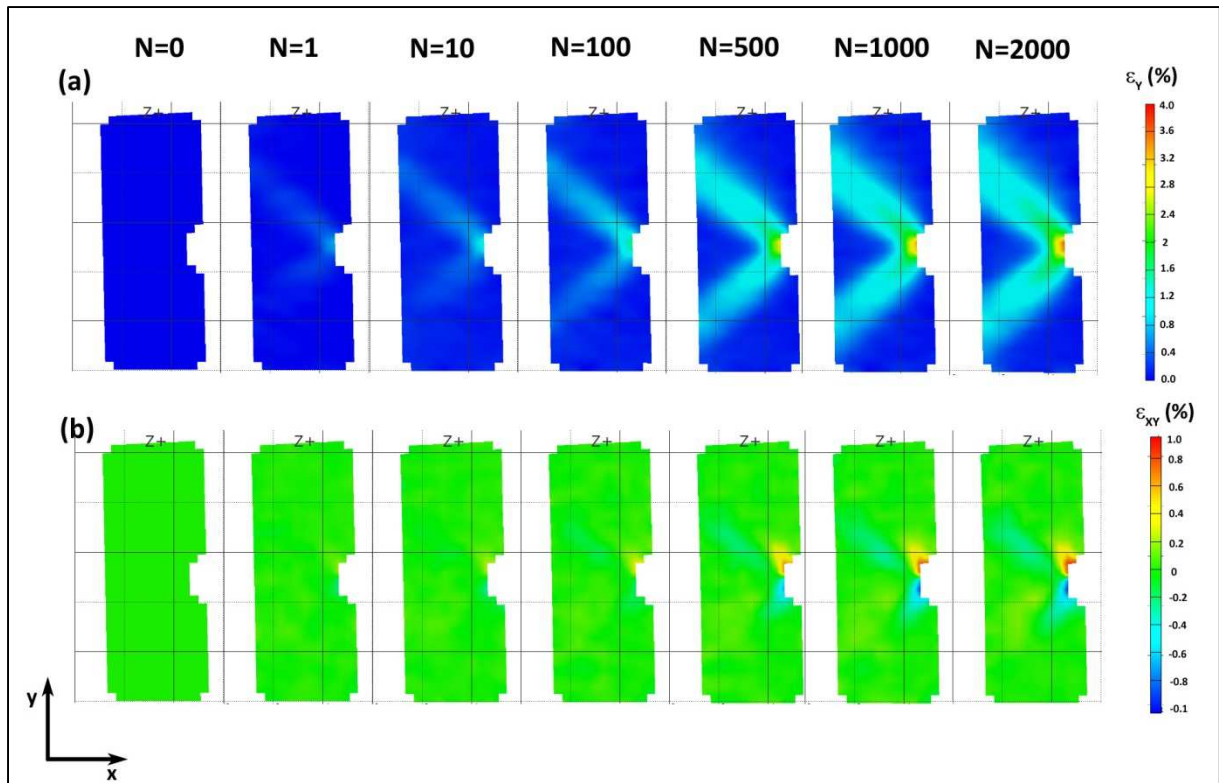
182 Note that the presence of a notch induces strain localisation and a behaviour different from the
183 one observed on smooth samples. Indeed, on a smooth specimen, until the propagation of the main
184 crack, the strain partition is more or less homogeneous. The resulting measurement by DIC would be
185 similar to the one obtained with a classical extensometer. In the current case, the most relevant
186 comparison with smooth samples is to consider an incremental step test method, which is generally
187 used to obtain a cyclic stress-strain curve. This test was performed under load control mode and the
188 strain was measured by an extensometer. Once the strain was stabilised, the step was finished and
189 the load was increased for the following loading step. The advantage of this test is that it needs only
190 one sample. However, it is important to specify a parameter for the end of a step which is
191 characterised by a stabilisation of the deformation during cycling. It is considered that the
192 stabilisation is reached when the difference between two cycles is inferior or equal to $10^{-4}/\text{cycle}$ as it
193 is shown in Figure 5a.

194 Table 1 summaries the results for the considered Fe-3Si steel. The obtained cyclic stress-strain curve
195 is represented in Figure 5b and compared with the monotonic tensile curve. A cyclic hardening is
196 observed and for a same stress, the strain is more important in monotonic loading than in cyclic
197 loading.

198 Hence, the value of 3% measured by DIC at the notch root after 2000 cycles results from the cycling
199 at a positive mean stress. When a material is subjected to such condition of loading, it is observed
200 that the hysteresis loops progressively shift toward positive value of strain and a steady state can be
201 observed or not. The latter case refers to the ratcheting effect and the total deformation
202 continuously increases [41]. When a steady state is observed, the total strain remains constant and
203 the stress-strain evolution evolve either in an elastic way or with plasticity. Figure 4b suggests that a
204 steady state has occurred, the loops do not shift anymore with increasing number of cycles since 500
205 cycles and very small plastic strain can be measured on the hysteresis loops. Therefore, the strain
206 value of 3 % results from an accumulation of cycles. Nevertheless, one may not exclude that the
207 strain at the notch tip resulting from each type of loading would be different from an equivalent
208 static loading. Indeed, the strain assessed by the DIC technique is only based on the processing of
209 displacement field. However, the microstructure behind will be different since the plasticity at the
210 notch root would activate differently the dislocation displacement.

211 Note that ratcheting effect also occurs during the incremental step test method. Moreover, the
212 behaviour of the steel in the localised deformation areas (as observed visually on Figure 4a)
213 corresponds to zones for which the material response is similar to regimes $\sigma_{ys} < \sigma_{max} < 1.2 \sigma_{ys}$.
214 Nevertheless, due to stress concentration effect, the associated strain amplitude is more
215 pronounced.

216 Then, in order to correlate these results in a more precise way, both EBSD and ECCI techniques are
217 necessary to be used to complete the DIC measurements otherwise incorrect plasticity mechanisms
218 may be proposed.



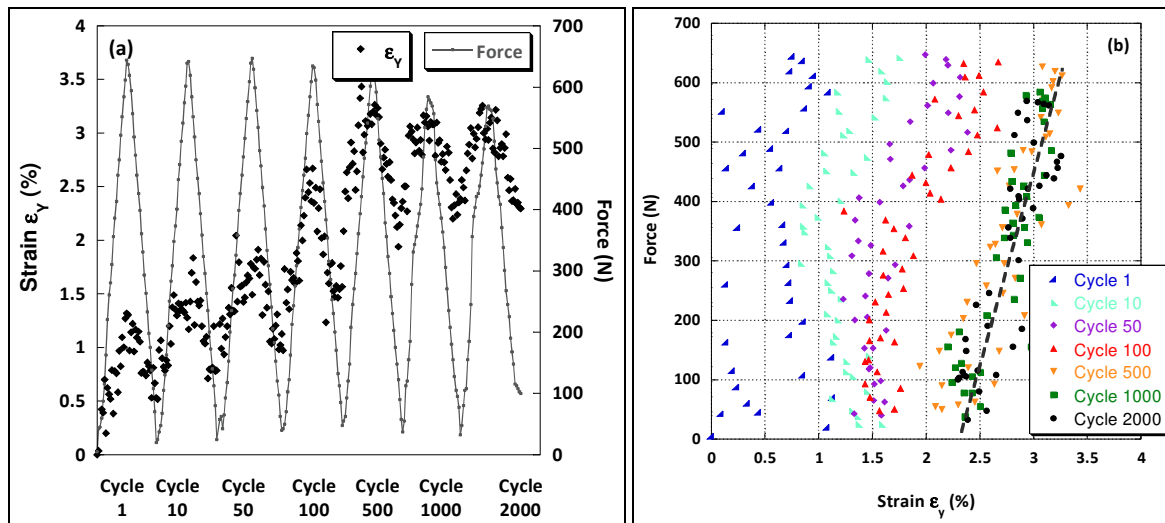
219

220 Figure 3: (a) Longitudinal strain, ϵ_y , and (b) shear strain, ϵ_{xy} , distribution estimation by DIC of a notched sample subjected to cyclic loading at F_{max} for cycle number $N=0, 1, 10, 100, 500, 1000$ and 2000

221

to cyclic loading at F_{max} for cycle number $N=0, 1, 10, 100, 500, 1000$ and 2000

222



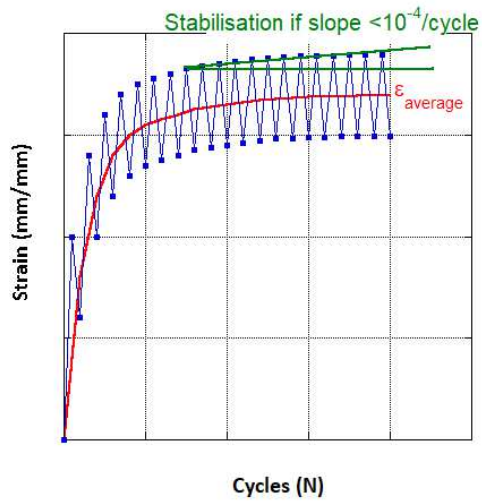
223

224 Figure 4: (a) Evolution of the longitudinal strain ϵ_y at the notch root and (b) hysteresis curves as a function of the cycle

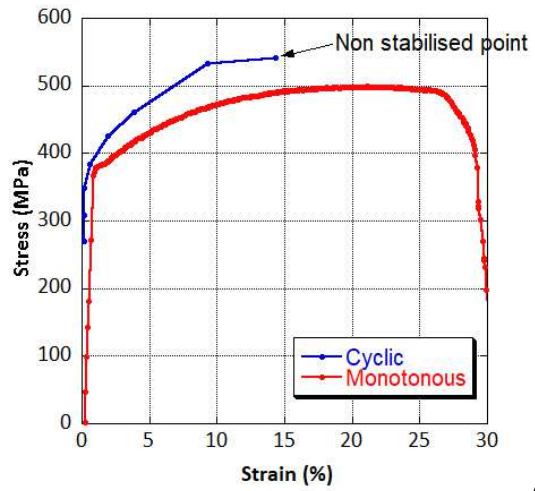
225

number

226



(a)



(b)

227

Figure 5: (a) Stabilisation criteria of a step (b) Cyclic vs monotonic stress-strain curve of the Fe-3Si steel

228

229

Table 1: Summary of the fatigue test by steps

230

σ_{\max}	Material response			Strain (stabilised regime)			Number of cycles to reach the stabilisation criteria
	σ_{\max} (MPa)	σ_{\min} (MPa)	σ_a (MPa)	ϵ_{\max} (%)	ϵ_{\min} (%)	$\Delta\epsilon_t$ (%)	
0.7 σ_{ys}	253	4.4	129.02	0.126	0.008	0.118	100
0.8 σ_{ys}	292	3.6	148	0.146	0.008	0.138	100
0.9 σ_{ys}	330	2	166.42	0.175	0.018	0.158	200
σ_{ys}	364	3.2	138.62	0.622	0.46	0.162	4000
1.1 σ_{ys}	403	1.2	202.22	1.89	1.69	0.2	4000
1.2 σ_{ys}	437	4.8	221.03	3.83	3.59	0.24	5000
1.3 σ_{ys}	495	29.6	262.4	9.31	9.02	0.29	500
1.4 σ_{ys}	508	7.2	257.83	15	14.7	0.34	Non stabilised

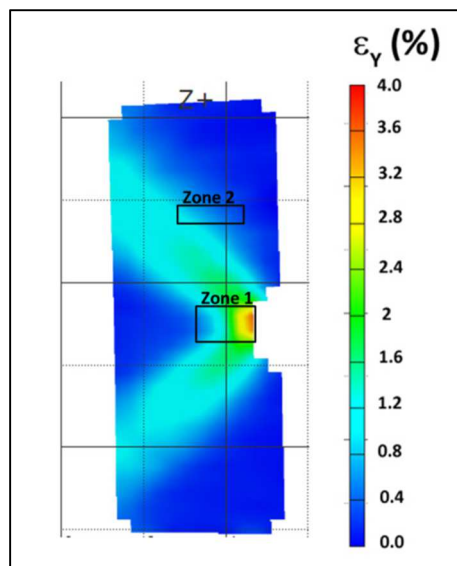
231

232

233

234 **3.2. EBSD analysis**

235 To highlight the ability of the EBSD tool to indicate the strain localisation effect, EBSD analyses were
236 carried out on the notched sample used for the study of strain distribution by DIC, at N=2000 cycles.
237 Figure 6 indicates the areas considered for the EBSD analysis on the normal strain distribution map
238 measured by DIC. The two considered zones are, for the first one, just behind the notch (zone 1) and
239 in the vicinity of a shear band (zone 2).



240

241 **Figure 6: Localisation of complementary EBSD analyses**

242

243 In order to have an overview of these broad areas, several maps of $800 \times 450 \mu\text{m}$ were recorded and
244 stitched to each other in order to form a global map of $1570 \times 750 \mu\text{m}^2$ (279 grains) for zone 1 and of
245 $3000 \times 815 \mu\text{m}^2$ (483 grains) for zone 2. The corresponding colour coded IPF, GROD and GOS maps
246 of zone 1 and zone 2 are shown in Figure 7 and Figure 8 respectively.

247 Both IPF, GROD and GOS maps of the zone 1 (figure 7) show orientation heterogeneities close to the
248 notch. For the IPF map (figure 7a), these heterogeneities correspond to local variation of the colour
249 contrast. The GROD map (figure 7b) shows that close to the notch (on the right) warmer colours are
250 obtained, which is the sign of higher misorientation (up to 8°) and strong localisation of orientation

251 heterogeneities at the grain boundaries. Further away from the notch, grain interiors become almost
252 free from misorientation gradients while those latter remain localised at the grain boundaries
253 vicinity.

254 The GOS map (figure 7c) attributes a grain colour that depends on the presence of misorientation
255 gradients within the grain. A gradient colour mapping is introduced: as the misorientation gradients
256 inside the grain become stronger, the colour evaluates from cold (blue, 0°) to warm (red, 5°) colours.

257 The EBSD investigation of the zone 1 shows that the grains become less misoriented away from the
258 notch. This observation is consistent with the strain localisation in this area. Indeed, strain is
259 correlated with the presence of both statistically stored dislocations (SSD) and geometrically
260 necessary dislocations (GND), and grain misorientation in deformed areas are inherited from their
261 presence. Moreover, the misorientation gradients observed inside the grain are consequences of
262 different dislocations signatures in the grain interior (vein structures) and at the grain boundary (wall
263 structures) [42].

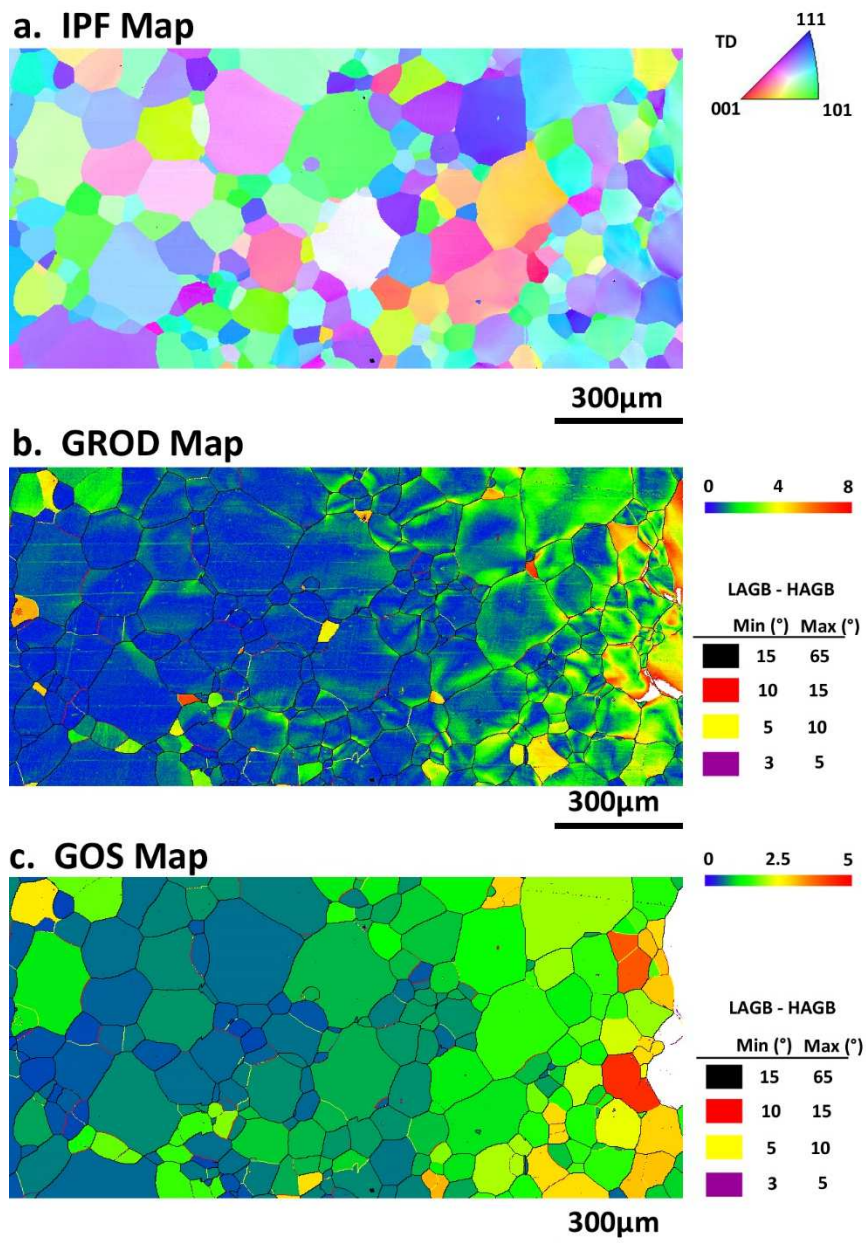
264 For further examinations and correlation with microstructure details and measured DIC values, the
265 global GOS map was divided in 4 subsets, defined with the black dot square areas of GOS map (figure
266 7c). The mean GOS, calculated in these subsets, are the following: $GOS_{mean,1}=1.55$, $GOS_{mean,2}=0.89$,
267 $GOS_{mean,3}=0.69$, $GOS_{mean,4}=0.6$.

268 Regarding the zone 2, on the left of the map (figure 8b), there is a slight misorientation gradient
269 within the grains, associated with a localisation at the grain boundary vicinity. Note that, some grains
270 exhibit higher misorientations levels. The trend is different on the right side of the map, for which
271 almost all the grains exhibit no misorientation gradient. This observation is confirmed by the GOS
272 map (figure 8c), which show a higher amount of grain free from misorientation gradient on the on
273 the right of the map. This observation is coherent with the DIC map (figure 6). Indeed, the presence
274 of the shear band which induces higher strain in the left part of the zone 2.

275 In this zone, the mean GOS (calculated from the black dot square area of the GOS map in figure 8) is
 276 0.62 and corresponds to the value $GOS_{mean,4}$ measured previously.

277 This quick comparison between, *i.* the DIC strain map of the notch sample at N=2000 cycles and *ii.*
 278 the localisation of the areas on which EBSD analysis has been carried out, confirms the ability of EBSD
 279 to emphasize the plastic strain localisation.

280



281

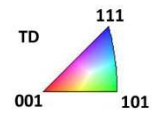
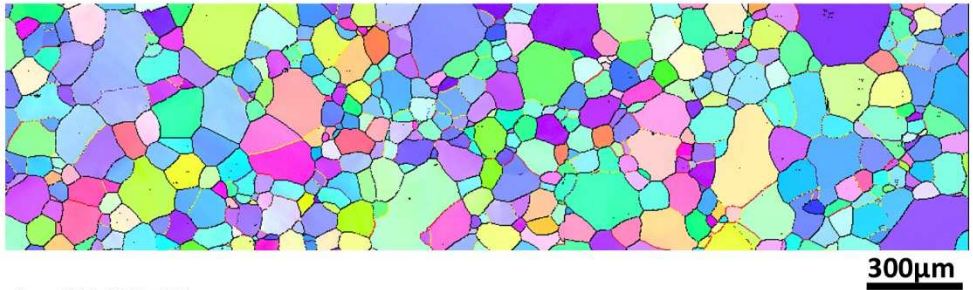
282

Figure 7: (a) IPF in TD direction, (b) GROD and (c) GOS maps of the Zone 1 of the sample (notch on the right)

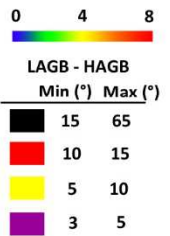
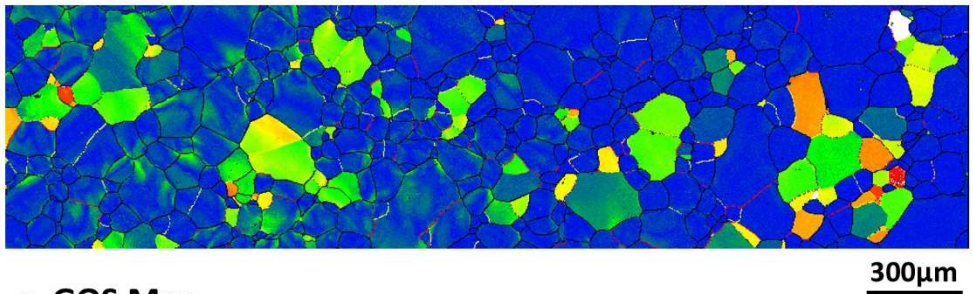
283

284

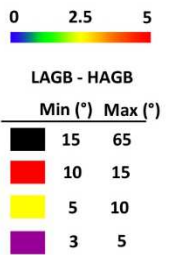
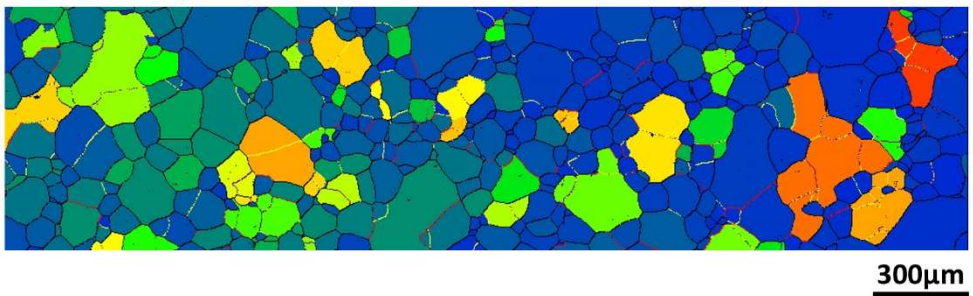
a. IPF Map



b. GROD Map



c. GOS Map



285

286

287

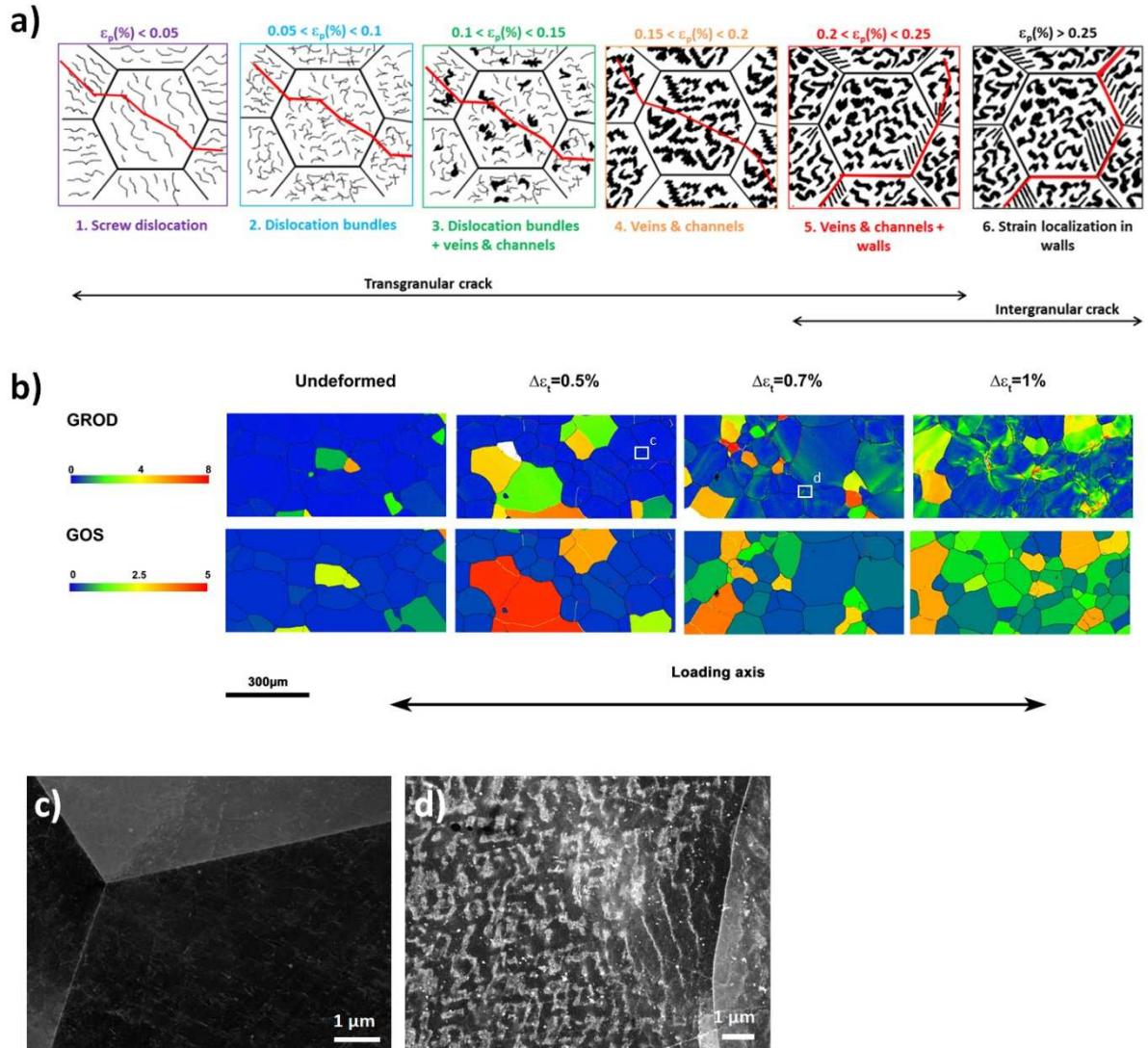
288

Figure 8: IPF in TD direction, GROD and GOS maps of the Zone 2 of the sample

289 **3.3. Deeper assessment of the cyclic plastic strain coupling EBSD, ECCI and DIC data**

290 As mentioned previously, the EBSD maps and corresponding measurements give a clear indication of
291 the strain localisation in the deformed notched sample. The LCF behaviour of the non-notched
292 samples has been fully investigated in previous works [32–34] and the obtained results are used to
293 correlate the strain levels measured with DIC and misorientations measured with EBSD for the
294 notched sample to an equivalent total strain variation of non – notched samples.

295 The main issues from these previous investigations are summarized in figure 9. As the total applied
296 strain increases, the Fe-3% Si steel exhibits behaviours equivalent to low temperature and to high
297 temperature regimes. For the lowest strain amplitudes, dislocation sources are activated within the
298 grain and dislocation slip is planar, as also reported for short range ordered alloys. While restricted
299 by high friction related to the Fe-Si clusters, the dislocation glide length remains sufficient to
300 accommodate the required strain in a quasi-static regime. This leads to transgranular cracking. By
301 contrast, for the highest level of deformation, plastic strains and cumulated strains can successfully
302 reduce the restricted effect of the Fe-Si short range order on the plasticity. Grains accommodate
303 individually plastic deformation, but dislocation glide through grains is difficult. The resulting
304 incompatibility effects produce intergranular stresses and strain localisation that generate
305 intergranular crack initiation (Figure 9a).



306

307 **Figure 9: (a) Schematic representation of dislocations structures involved in the damage of the Fe-Si steel (b) Evolution of**
 308 **the GROD and GOS maps for LCF test on smooth specimens as a function of the applied strain (c) and (d) corresponding**
 309 **ECCI observations**

310

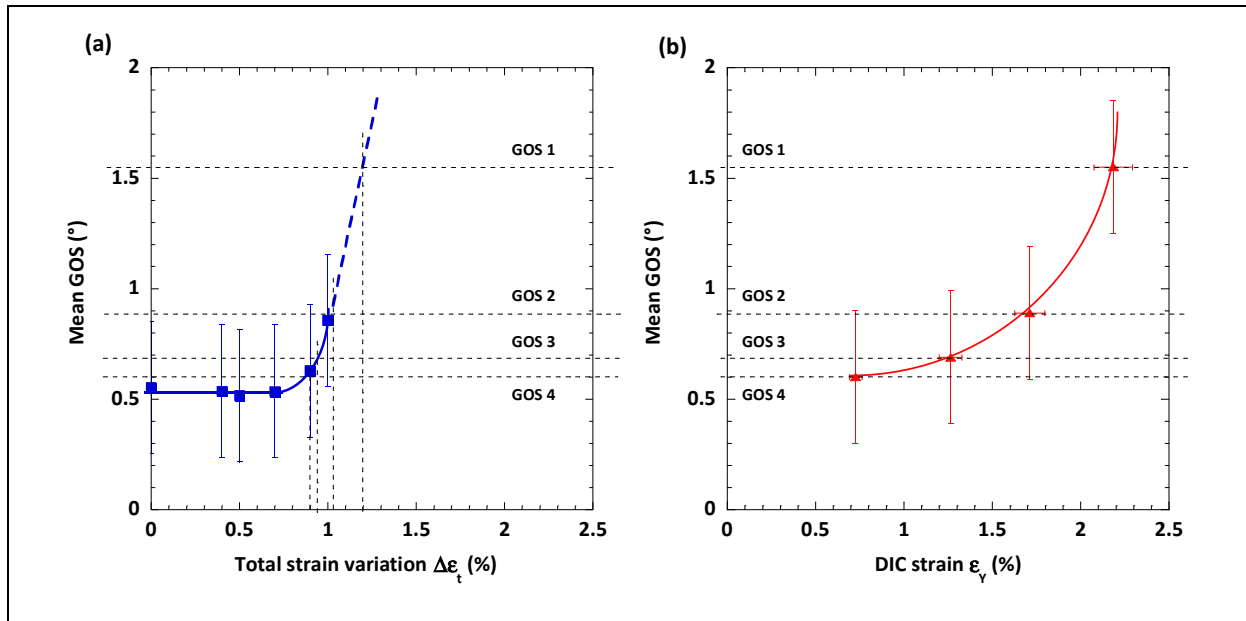
311 This strain accommodation was suggested from EBSD data processing and imaged by ECCI and two
 312 major conclusions were highlighted (Figure 9b, 9c and 9d). Firstly, the strain accommodation with the
 313 grains is associated by the formation of dislocation structures commonly described in fatigue [43–
 314 45]. Nevertheless, due to the stress incompatibility at the grain boundary, the corresponding strain
 315 localisation results in variation of dislocations structure between the grain interiors (vein and
 316 channels) and the vicinity of the grain boundary (walls). This difference can be clearly evaluated in

317 terms of misorientations, since veins consists of an agglomeration of edge dipoles, surrounded by
318 GNDs. By contrast, channels only exhibit very few SSDs. In addition, walls are veins evolutions for
319 which edge dipoles accumulate and then confine while misorientation increases [42,46–48]. Here
320 both step size and angular resolution, considered in the present analysis, do not permit a fine
321 distinction between dislocations rich veins/walls zones and channels. Nevertheless the transition
322 between veins/channels and walls results in gradients that were clearly observed through the GROD
323 criterion [32,49].

324 On the second hand, a clear correlation between the appearance of a strain localisation as a function
325 of the applied strain level has been evaluated by taking into account the GOS criterion. Indeed, such
326 a strain localisation is correlated to misorientation gradients at the grain interfaces. The deeper the
327 walls structures spread inside the grains, the higher become the gradient. In addition, the number of
328 grains for which such a localisation effect occur also increases with higher total strain levels.

329 From these observations, there is a way to estimate the equivalent strain undergone by the
330 material in the different areas of zone 1 based on the relation established in figure 10 (a) in which
331 the mean GOS value is correlated to the total strain variation. A numerical correlation is done for an
332 estimation of the GOS value corresponding to $\Delta\varepsilon_t > 1.0\%$.

333 Therefore, the mean GOS values previously measured on the notched specimen in zone 1 are
334 reported in Figure 10 (a) and the equivalent total strain variations are deduced by graphical reading.
335 In addition, these mean GOS values are plotted against the normal local strain value obtained by DIC
336 in Figure 10 (b).



337

338

339

340

341

342

343

344

345

346

347

348

349

350

351

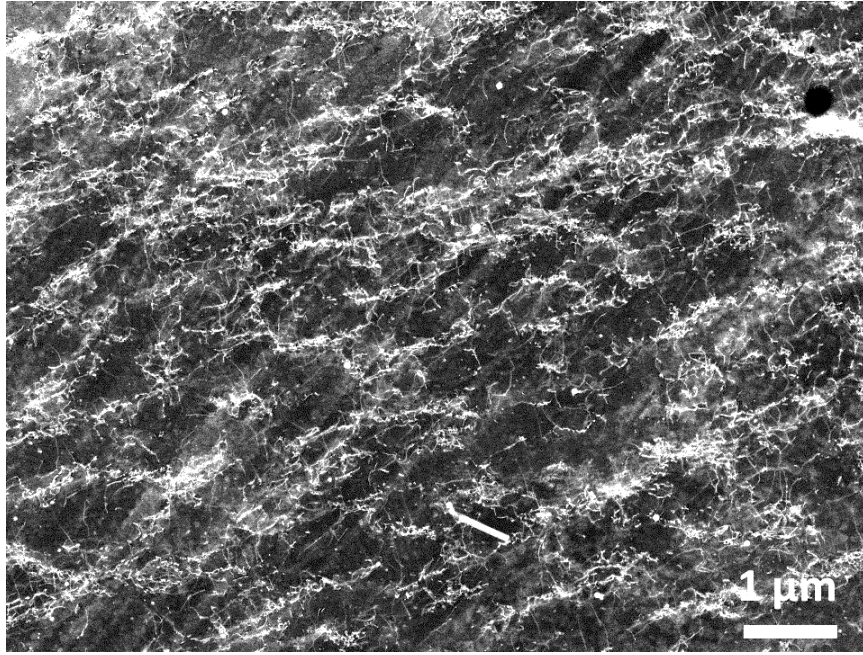
Figure 10: (a) Equivalent total strain estimation in the different zones of the notched specimen from the relation

between GOS and total strain variation established on smooth specimen and (b) mean GOS value of the different zones

of the notched specimen versus the normal strain measured by DIC

It can be noticed here that a direct correspondence of the normal strain calculated by DIC on the notched sample with the total strain variation of the smooth samples is difficult and more especially for the highest strains. Indeed, the LCF study on smooth samples was performed only up to $\Delta\epsilon_t=1\%$. Above this strain range, the dislocation structure and mean GOS value in the case of smooth sample are unknown. Also, a precise estimation of the strain by the GOS criteria over a small area is difficult because large grain size hinders statistical analyses and strain measurements by DIC are made on a macroscopic scale.

The observation of the dislocation structure in area 1 of zone 1 (zone where highest strains are reached) by ECCI is shown in Figure 11. It reveals irregular dislocation walls in the process of transforming into dislocation cells.



352

353

Figure 11: ECCL micrograph of the dislocation structure near the notch

354

This structure expresses a more advanced deformation state than those observed in smooth samples

355

loaded at $\Delta\varepsilon_t=1\%$. Therefore, this is consistent with the fact that in area 1, strains superior to the

356

equivalent total strain variation of 1% are reached and that a ratcheting effect, leading to mean

357

strain of 3% is observed.

358

Furthermore, referring to these new results, one possible evolution of mean GOS as a function of

359

total strain variation is shown in Figure 12. In this figure, the GOS evolution with the total strain

360

variation is depicted in three stages. During the first stage, the mean GOS is constant over a wide

361

strain range (from $\Delta\varepsilon_t=0\%$ to $\Delta\varepsilon_t=0.7\%$) because the dislocation structure is homogeneous in the

362

grain. During the second stage, the mean GOS increases rapidly with the total strain variation (from

363

$\Delta\varepsilon_t=0.7\%$ to $\Delta\varepsilon_t=1\%$), this is due to localisation of the strain at grain boundary and higher

364

misorientation in this zone.

365

The linear increase of the mean GOS with $\Delta\varepsilon_t$ reflects the increasing ratio between dipolar walls in

366

the vicinity of grain boundaries and veins in the grain interiors. When the grain is completely filled

367

out with walls, an increase in strain should trigger the transformation of walls into cells. A new

368

regime, the third stage, takes then place.

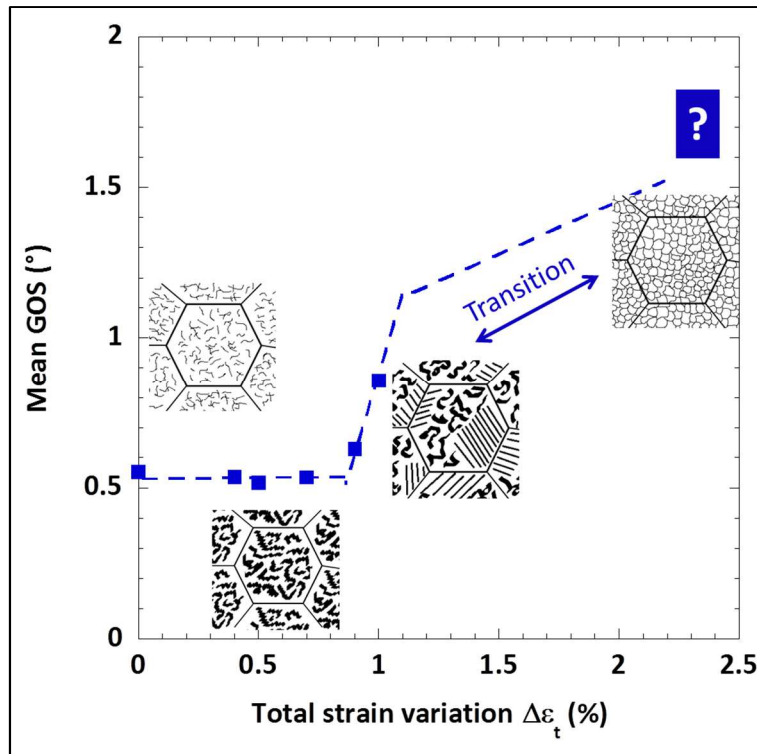


Figure 12: Evolution of mean GOS with total strain variation

369

370

371

372 The proposed approach, based on a comparison between GROD/GOS misorientation criteria and
 373 linked with DIC measurements and ECCI imaging, differs from the current approaches developed
 374 around EBSD, ECCI and DIC. Although the selected EBSD acquisition parameters (step size, EBSD
 375 resolution) do not permit to detail locally the Nye tensor and calculate precisely the dislocations
 376 densities by lacking of both high spatial resolution and high angular resolution, it allows the
 377 comparison of different zones in the sample and propose a clear view of the local plasticity levels.

378 Indeed, the major trends of the new EBSD developments are based on high resolution EBSD (HR-
 379 EBSD) or Cross-Correlation EBSD (CC-EBSD). Nevertheless, most of the works do not face directly the
 380 calculated GNDs densities, distributions and stress/strain fields with corresponding dislocations
 381 structures for FCC structures (single phase copper and nickel alloys) [30,50,51]. A more recent
 382 approach makes a comparison between cECCI and CC-EBSD in order to explain how entangled
 383 dislocations evolve to wall and channels structure in a DP steel [52]. However, in that latter case, a

384 huge amount of data, coupled with a fine step size in terms of EBSD acquisition are required.
385 Although the corresponding results are highly valuable and bring microscopic details on how the
386 microstructure evolve during cycling, the scale limitation remains restraint when taking into account
387 a large zone with a possible variation in terms of dislocations structuration as observed in the
388 present study.

389 The same kind of observation can be done for DIC measurements, as for cyclic plasticity, the
390 measurements are mainly related to the residual strains or the maximum strains, depending on how
391 and when the data are acquired.

392

393 **Conclusions**

394 The current work aimed at proposing a judicious combination of microscopy related measurements
395 and observations to understand in both qualitative and quantitative ways the effect of cyclic loading
396 on the microstructure response of a Fe-3%Si steel. Three complementary techniques have been
397 considered: EBSD, ECCI and DIC.

398 Although each of the techniques is well known and its application to plastic strain determination well
399 documented in the literature, some considerations have to be taken into account.

- 400 • EBSD analysis, conducting with right selected parameters, can lead to a clear overview of the
401 plastic strain. However, a particular attention has to be done when post-processing the data.
402 In general, EBSD data are only linked to misorientation and pattern quality measurements.
403 The first aspect indirectly characterises the GND dislocations, while the second may be
404 related with both GND and SSD dislocations. The corresponding strain and stress field can
405 also derivate from the misorientation measurements, but the acquisition step-size is of prime
406 importance.

407 • ECCI gives a clear observation of the dislocations, as these latter would be observed by TEM.
408 However, this technique cannot make a distinction between SSDs and GNDs.

409 • Strain fields obtained through DIC measurements are easily understood. When characterising
410 the strain fields coming from a cyclic loading, the situation appears to be a bit more complex.

411 The combination of the data coming from the three different techniques avoid to make some
412 mistakes. The misorientation criteria obtained with EBSD can easily be associated to dislocations
413 structuration, as comparing with ECCI observations. In a same manner, such measurements can also
414 be related to strain levels determined by DIC.

415 Applied on a notched specimen made of Fe-3%Si steel, submitted to cyclic loading, new details on
416 the materials behaviour have been obtained.

417 The DIC measurements clearly emphasise the strain localisation effect during cycling. In addition, it
418 points out a ratcheting effect, which is more pronounced close to the notch. However, taking into
419 account the resulting deformation measurement from the DIC data alone does not reflect the
420 accumulated plasticity of the material. Hence, the use of abacuses, linking local misorientation and
421 total strain variation, on one hand and misorientation and the DIC measurements of residual cyclic
422 strain on the other hand, confirms a higher accumulated cyclic strain in the notch region, which can
423 be related to the combination of a higher strain amplitude with a higher mean strain. This has also
424 been confirmed by the ECCI observations that show irregular dislocation walls in the process of
425 transforming into dislocation cells.

426

427 **Acknowledgment**

428 The authors thank Valeo France for Financial support, Mr. Golek and Mr. Creton for the technical
429 help. The SEM facility in Lille (France) is supported by the Conseil Régional du Nord-Pas de Calais,
430 and the European Regional Development Fund (ERDF).

431

432

433 **Data availability statement**

434 The raw/processed data required to reproduce these findings cannot be shared at this time due to

435 legal or ethical reasons

436

437

438 **References**

- 439 [1] W. Zhang, Y. Zhang, H. Li, X. Gu, Experimental investigation of fatigue bond behavior between
440 deformed steel bar and concrete, *Cem. Concr. Compos.* 108 (2020) 103515.
441 doi:10.1016/j.cemconcomp.2020.103515.
- 442 [2] M. Tripathi, R.P. Dhakal, F. Dashti, L.M. Massone, Low-cycle fatigue behaviour of reinforcing
443 bars including the effect of inelastic buckling, *Constr. Build. Mater.* 190 (2018) 1226–1235.
444 doi:10.1016/j.conbuildmat.2018.09.192.
- 445 [3] J.-B. Vogt, C. Carle, J. Bouquerel, I. Proriol Serre, Behaviour of short and long cracks in air and
446 in liquid metal in T91 steel, in: *MATEC Web Conf.*, 2018.
447 doi:10.1051/matecconf/201816503016.
- 448 [4] J.B. Vogt, S. Argillier, J.P. Massoud, V. Prunier, Fatigue damage evaluation of a power plant
449 component from analysis of the dislocation structures, *Eng. Fail. Anal.* 7 (2000) 301–310.
450 doi:10.1016/S1350-6307(99)00034-5.
- 451 [5] M. Shirani, G. Härkegård, A review on fatigue design of heavy section EN-GJS-400-18-LT
452 ductile iron wind turbine castings, *Energy Equip. Syst.* 2 (2014) 5–24.
453 doi:10.22059/ees.2014.5008.
- 454 [6] R. Branco, J.D. Costa, F. Berto, A. Kotousov, F. V. Antunes, Fatigue crack initiation behaviour of
455 notched 34CrNiMo6 steel bars under proportional bending-torsion loading, *Int. J. Fatigue.*
456 (2020). doi:10.1016/j.ijfatigue.2019.105268.
- 457 [7] F.M. Firouz, E. Mohamed, A. Lotfy, A. Daoud, M.T. Abou El-Khair, Thermal expansion and
458 fatigue properties of automotive brake rotor made of AlSi–SiC composites, *Mater. Res.*
459 *Express.* 6 (2020) 1265d2. doi:10.1088/2053-1591/ab6129.
- 460 [8] M. Fonte, P. Duarte, V. Anes, M. Freitas, L. Reis, On the assessment of fatigue life of marine
461 diesel engine crankshafts, *Eng. Fail. Anal.* 56 (2015) 51–57.

- 462 doi:10.1016/j.engfailanal.2015.04.014.
- 463 [9] Z. Zheng, S. Yuan, T. Sun, S. Pan, Fractographic study of fatigue cracks in a steel car wheel,
464 Eng. Fail. Anal. 47 (2015) 199–207. doi:10.1016/j.engfailanal.2014.09.010.
- 465 [10] S.M.O. Tavares, P.M.S.T. de Castro, An overview of fatigue in aircraft structures, Fatigue Fract.
466 Eng. Mater. Struct. 40 (2017) 1510–1529. doi:10.1111/ffe.12631.
- 467 [11] L. Li, A. Kedous-Lebouc, A. Foggia, J.C. Mipo, Influence of magnetic materials on claw pole
468 machines behavior, IEEE Trans. Magn. 46 (2010) 574–577. doi:10.1109/TMAG.2009.2032520.
- 469 [12] G. Cai, C. Li, B. Cai, Q. Wang, An investigation on the role of texture evolution and ordered
470 phase transition in soft magnetic properties of Fe–6.5 wt%Si electrical steel, J. Magn. Magn.
471 Mater. 430 (2017) 70–77. doi:10.1016/j.jmmm.2017.01.054.
- 472 [13] M. Reinlein, T. Hubert, A. Hoffmann, A. Kremser, Optimization of analytical iron loss
473 approaches for electrical machines, 2013 3rd Int. Electr. Drives Prod. Conf. EDPC 2013 - Proc.
474 (2013) 1–7. doi:10.1109/EDPC.2013.6689759.
- 475 [14] F. Henrotte, S. Steentjes, K. Hameyer, C. Geuzaine, Iron loss calculation in steel laminations at
476 high frequencies, IEEE Trans. Magn. 50 (2014) 0–3. doi:10.1109/TMAG.2013.2282830.
- 477 [15] M. Sugiyama, M. Shibata, Application of Scanning Electron Microscope to Dislocation Imaging
478 in Steel, JEOL News. 46 (2011) 11–16. <http://www.jeol.co.jp/en/applications/detail/780.html>.
- 479 [16] S. Zaefferer, N.-N. Elhami, Theory and application of electron channelling contrast imaging
480 under controlled diffraction conditions, Acta Mater. 75 (2014) 20–50.
481 doi:10.1016/j.actamat.2014.04.018.
- 482 [17] J. Jiang, T.B. Britton, A.J. Wilkinson, Evolution of dislocation density distributions in copper
483 during tensile deformation, Acta Mater. 61 (2013) 7227–7239.
484 doi:10.1016/j.actamat.2013.08.027.

- 485 [18] J. Jiang, T.B. Britton, A.J. Wilkinson, Measurement of geometrically necessary dislocation
486 density with high resolution electron backscatter diffraction: Effects of detector binning and
487 step size, *Ultramicroscopy*. 125 (2013) 1–9. doi:10.1016/j.ultramic.2012.11.003.
- 488 [19] M. Hayakawa, M. Wakita, E. Nakayama, Damage evaluation of ferrite and ferrite-pearlite steel
489 during fatigue crack initiation by EBSD, *Adv. Mater. Res.* 891–892 (2014) 410–415.
490 doi:10.4028/www.scientific.net/AMR.891-892.410.
- 491 [20] M.J. Holzweissig, P. Kanagarajah, H.J. Maier, Digital image correlation at high temperatures
492 for fatigue and phase transformation studies, *J. Strain Anal. Eng. Des.* 49 (2014) 204–211.
493 doi:10.1177/0309324713498737.
- 494 [21] A.D. Darbal, M. Gemmi, J. Portillo, E. Rauch, S. Nicolopoulos, Nanoscale Automated Phase and
495 Orientation Mapping in the TEM, *Micros. Today*. 20 (2012) 38–42.
496 doi:10.1017/S1551929512000818.
- 497 [22] C. Rehrl, S. Kleber, T. Antretter, R. Pippan, A methodology to study crystal plasticity inside a
498 compression test sample based on image correlation and EBSD, *Mater. Charact.* 62 (2011)
499 793–800. doi:10.1016/j.matchar.2011.05.009.
- 500 [23] G. L’hôte, C. Lafond, P. Steyer, S. Deschanel, T. Douillard, C. Langlois, S. Cazottes, Rotational-
501 Electron Channeling Contrast Imaging analysis of dislocation structure in fatigued copper
502 single crystal, *Scr. Mater.* 162 (2019) 103–107. doi:10.1016/j.scriptamat.2018.10.050.
- 503 [24] M.T. Welsch, M. Henning, M. Marx, H. Vehoff, Measuring the plastic zone size by Orientation
504 Gradient Mapping (OGM) and Electron Channeling Contrast Imaging (ECCI), *Adv. Eng. Mater.* 9
505 (2007) 31–37. doi:10.1002/adem.200600195.
- 506 [25] T. Niendorf, J. Dadda, D. Canadinc, H.J. Maier, I. Karaman, Monitoring the fatigue-induced
507 damage evolution in ultrafine-grained interstitial-free steel utilizing digital image correlation,
508 *Mater. Sci. Eng. A*. 517 (2009) 225–234. doi:10.1016/j.msea.2009.04.053.

- 509 [26] A. Guery, F. Hild, F. Latourte, S. Roux, Slip activities in polycrystals determined by coupling DIC
510 measurements with crystal plasticity calculations, *Int. J. Plast.* 81 (2016) 249–266.
511 doi:10.1016/j.ijplas.2016.01.008.
- 512 [27] W. Abuzaid, H. Sehitoglu, J. Lambros, Plastic strain localization and fatigue micro-crack
513 formation in Hastelloy X, *Mater. Sci. Eng. A.* 561 (2013) 507–519.
514 doi:10.1016/j.msea.2012.10.072.
- 515 [28] E. Salvati, S. O’Connor, T. Sui, D. Nowell, A.M. Korsunsky, A study of overload effect on fatigue
516 crack propagation using EBSD, FIB–DIC and FEM methods, *Eng. Fract. Mech.* 167 (2016) 210–
517 223. doi:10.1016/j.engfracmech.2016.04.034.
- 518 [29] J. Nellesen, S. Sandlöbes, D. Raabe, Effects of strain amplitude, cycle number and orientation
519 on low cycle fatigue microstructures in austenitic stainless steel studied by electron
520 channelling contrast imaging, *Acta Mater.* 87 (2015) 86–99.
521 doi:10.1016/j.actamat.2014.12.024.
- 522 [30] T. Zhang, J. Jiang, B. Britton, B. Shollock, F. Dunne, Crack nucleation using combined crystal
523 plasticity modelling, high-resolution digital image correlation and high-resolution electron
524 backscatter diffraction in a superalloy containing non-metallic inclusions under fatigue, *Proc.*
525 *R. Soc. A Math. Phys. Eng. Sci.* 472 (2016). doi:10.1098/rspa.2015.0792.
- 526 [31] F. Bridier, J.C. Stinville, N. Vanderesse, P. Villechaise, P. Bocher, Microscopic strain and crystal
527 rotation measurement within metallurgical grains, *Key Eng. Mater.* 592–593 (2014) 493–496.
528 doi:10.4028/www.scientific.net/KEM.592-593.493.
- 529 [32] C. Schayes, J. Bouquerel, J.-B. Vogt, F. Palleschi, S. Zaefferer, A comparison of EBSD based
530 strain indicators for the study of Fe-3Si steel subjected to cyclic loading, *Mater. Charact.* 115
531 (2016). doi:10.1016/j.matchar.2016.03.020.
- 532 [33] C. Schayes, J.-B. Vogt, J. Bouquerel, F. Palleschi, S. Zaefferer, Cyclic plasticity mechanism of the

- 533 M330-35A steel, *Int. J. Fatigue*. 82 (2016). doi:10.1016/j.ijfatigue.2015.09.008.
- 534 [34] C. Schayes, J.-B. Vogt, J. Bouquerel, F. Palleschi, Rotor Design Optimisation through Low Cycle
535 Fatigue Testing, in: *Procedia Eng.*, 2015. doi:10.1016/j.proeng.2015.12.663.
- 536 [35] M.F. De Campos, F.J.G. Landgraf, R. Takanohashi, F.C. Chagas, I.G.S. Falleiros, G.C. Fronzaglia,
537 H. Kahn, Effect of the hot band grain size and intermediate annealing on the deformation and
538 recrystallization textures in low silicon electrical steels, *ISIJ Int.* 44 (2004) 591–597.
539 doi:10.2355/isijinternational.44.591.
- 540 [36] M.F. de Campos, F.J.G. Landgraf, I.G.S. Falleiros, G.C. Fronzaglia, H. Kahn, Texture Evolution
541 during the Processing of Electrical Steels with 0.5% Si and 1.25% Si, *ISIJ Int.* 44 (2004) 1733–
542 1737. doi:10.2355/isijinternational.44.1733.
- 543 [37] M.A. da Cunha, S. da C. Paolinelli, Low core loss non-oriented silicon steels, *J. Magn. Magn.*
544 *Mater.* 320 (2008) 2485–2489. doi:10.1016/j.jmmm.2008.04.054.
- 545 [38] A. Ramazani, A. Schwedt, A. Aretz, U. Prahl, W. Bleck, Characterization and modelling of
546 failure initiation in DP steel, *Comput. Mater. Sci.* 75 (2013) 35–44.
547 doi:10.1016/j.commatsci.2013.04.001.
- 548 [39] N. McCormick, J. Lord, Digital image correlation, *Mater. Today*. 13 (2010) 52–54.
549 doi:10.1016/S1369-7021(10)70235-2.
- 550 [40] Y. Chen, J. Hjelen, S.S. Gireesh, H.J. Roven, Optimization of EBSD parameters for ultra-fast
551 characterization, *J. Microsc.* 245 (2012) 111–118. doi:10.1111/j.1365-2818.2011.03551.x.
- 552 [41] S.K. Paul, A critical review of experimental aspects in ratcheting fatigue: Microstructure to
553 specimen to component, *J. Mater. Res. Technol.* 8 (2019) 4894–4914.
554 doi:10.1016/j.jmrt.2019.06.014.
- 555 [42] H. Mughrabi, Dual role of deformation-induced geometrically necessary dislocations with

556 respect to lattice plane misorientations and/or long-range internal stresses, *Acta Mater.* 54
557 (2006) 3417–3427. doi:10.1016/j.actamat.2006.03.047.

558 [43] F. Ackermann, L.P. Kubin, J. Lepinoux, H. Mughrabi, The dependence of dislocation
559 microstructure on plastic strain amplitude in cyclically strained copper single crystals, *Acta*
560 *Metall.* 32 (1984) 715–725. doi:10.1016/0001-6160(84)90145-7.

561 [44] H. Mughrabi, K. Herz, X. Stark, Cyclic deformation and fatigue behaviour of alpha-iron mono-
562 and polycrystals, *Int. J. Fract.* 17 (1981) 193–220. doi:10.1007/BF00053520.

563 [45] D. Kuhlmann-Wilsdorf, C. Laird, Dislocation behavior in fatigue, *Mater. Sci. Eng.* 27 (1977)
564 137–156. doi:10.1016/0025-5416(77)90166-5.

565 [46] H. Mughrabi, Deformation-induced long-range internal stresses and lattice plane
566 misorientations and the role of geometrically necessary dislocations, *Philos. Mag.* 86 (2006)
567 4037–4054. doi:10.1080/14786430500509054.

568 [47] A. Irastorza-Landa, H. Van Swygenhoven, S. Van Petegem, N. Grilli, A. Bollhalder, S.
569 Brandstetter, D. Grolimund, Following dislocation patterning during fatigue, *Acta Mater.* 112
570 (2016) 184–193. doi:10.1016/j.actamat.2016.04.011.

571 [48] A. Irastorza-Landa, N. Grilli, H. Van Swygenhoven, Effect of pre-existing immobile dislocations
572 on the evolution of geometrically necessary dislocations during fatigue, *Model. Simul. Mater.*
573 *Sci. Eng.* 25 (2017). doi:10.1088/1361-651X/aa6e24.

574 [49] W. Pantleon, Resolving the geometrically necessary dislocation content by conventional
575 electron backscattering diffraction, *Scr. Mater.* 58 (2008) 994–997.
576 doi:10.1016/j.scriptamat.2008.01.050.

577 [50] J. Jiang, J. Yang, T. Zhang, F.P.E. Dunne, T. Ben Britton, On the mechanistic basis of fatigue
578 crack nucleation in Ni superalloy containing inclusions using high resolution electron
579 backscatter diffraction, *Acta Mater.* 97 (2015) 367–379. doi:10.1016/j.actamat.2015.06.035.

- 580 [51] J. Jiang, T.B. Britton, A.J. Wilkinson, Evolution of intragranular stresses and dislocation
581 densities during cyclic deformation of polycrystalline copper, *Acta Mater.* 94 (2015) 193–204.
582 doi:10.1016/j.actamat.2015.04.031.
- 583 [52] D. An, S. Zaefferer, Formation mechanism of dislocation patterns under low cycle fatigue of a
584 high-manganese austenitic TRIP steel with dominating planar slip mode, *Int. J. Plast.* 121
585 (2019) 244–260. doi:10.1016/j.ijplas.2019.06.009.
- 586